NANO · MICRO small
www.small-journal.com

Multilevel Resistive Switching Dynamics by Controlling Phase and Self-Assembled Nanochannels in HfO_2

*Tanmayee Parida, Minh Anh Luong, Santanu Das, Alain Claverie, and Aloke Kanjilal**

A resistive switching device with precise control over the formation of conductive filaments (CF) holds immense potential for high-density memory arrays and atomic-scale in-memory computing architectures. While ion migration and electrochemical switching mechanisms are well understood, controlling the evolution of CF remains challenging for practical resistive random-access memory (RRAM) deployment. This study introduces a systematic approach to modulate oxygen vacancies (OV) in HfO_2 films of Ag/HfO_2/Pt-based RRAM devices by controlling the substrate temperature. At 300 °C, the HfO_2 film exhibits a dominant monoclinic phase with maximum OV concentration, which plays a key role in achieving optimal multilevel resistive switching behavior. Self-assembled nanochannels in the HfO_2 films guide CF evolution, and the diffusion of Ag at inside these films suggests a synergistic interplay between OV and Ag^+ ion migration for reseting the voltage-controlled resistive states. This approach addresses the endurance/retention trade-off with an impressive R_{on}/R_{off} ratio of ≈8000 while demonstrating growth temperature-driven OV modulation as a tool for multi-bit data storage. These findings provide a blueprint for developing high-performance oxide-based RRAM devices and offer valuable insights into multilevel resistive switching mechanisms, paving the way for future low-power, high-density memory technologies.

1. Introduction

Resistive random-access memory (RRAM) is increasingly recognized as a frontrunner for next-generation non-volatile memory and neuromorphic computing, owing to its potential for ultra-low power consumption, fast switching speeds, and high scalability.[1–6] However, the challenge of achieving stable and reproducible multilevel resistive switching remains a key hurdle.[5,7–9] To address this, precise control over the microstructure and defect states is essential, as these factors directly influence the resistive switching characteristics. In particular, engineering oxygen vacancies (OV) and their involvement in the formation of conductive filaments (CF) within the dielectric matrix are critical for enabling reliable multi-bit data storage.[10,11]

Among different metal oxides, hafnium oxide (HfO_2) is considered to be a promising high-k material for energy efficient RRAM applications due to its excellent structural and chemical properties,[12] where the OV play a significant role for low current/voltage operation with a device-to-device uniformity and scalability. Its high dielectric constant and excellent thermal stability not only make it favorable for achieving multilevel behavior in RRAM devices towards neuromorphic applications, but also for their compatibility in direct integration into the existing semiconductor technology. However, achieving optimal performance in HfO_2-based RRAM devices demands innovative approaches in the formation of CF since precise control of the filament makes it possible to store more information in each device. This leads to multilevel cells and better synaptic devices for neuromorphic computing,[13–16] though the formation of CF in RRAM devices is often complex and influenced by various factors. The composition of these filaments can change significantly based on the controlling parameters of the devices.[17] Numerous efforts have been made to better understand this process for practical RRAM applications. For instance, Lee et al.[2] showed a dual-mode switching mechanism with the coexistence of Ag and OV-driven filament formation in an Ag/Ta_2O_5/Pt device, controlling the configuration of the filament by varying compliance current (CC). Moreover, Jeong et al.[18] investigated the influence of grain sizes on the dynamics associated with CF. An interesting article by Niu et al.[19] used electron holography in transmission electron microscopy (TEM) for direct observation of CF to unveil their physical nature. Chang et al.[20] again suggested the involvement of dual filament switching in Ta_2O_5 memristors and demonstrated the forming process using TEM. However, Jiang et al.[21] demonstrated the superior switching behavior in HfO_2-based devices due to the involvement a sub-10 nm Ta channel.

T. Parida, A. Kanjilal
Department of Physics
School of Natural Sciences
Shiv Nadar Institution of Eminence
Gautam Buddha Nagar, Uttar Pradesh 201314, India
E-mail: aloke.kanjilal@snu.edu.in

M. A. Luong, A. Claverie
CEMES-CNRS and Universite de Toulouse
29 rue J. Marvig
Toulouse 31055, France

S. Das
Department of Ceramic Engineering
Indian Institute of Technology (BHU)
Varanasi, Uttar Pradesh 221005, India

The ORCID identification number(s) for the author(s) of this article can be found under https://doi.org/10.1002/smll.202409798

DOI: 10.1002/smll.202409798

 © 2024 Wiley-VCH GmbH

16136829, 2025, 7, Downloaded from https://onlinelibrary.wiley.com/doi/10.1002/smll.202409798 by Indian Institute Of Technology, Wiley Online Library on [05/06/2026]. See the Terms and Conditions (https://onlinelibrary.wiley.com/terms-and-conditions) on Wiley Online Library for rules of use; OA articles are governed by the applicable Creative Commons License

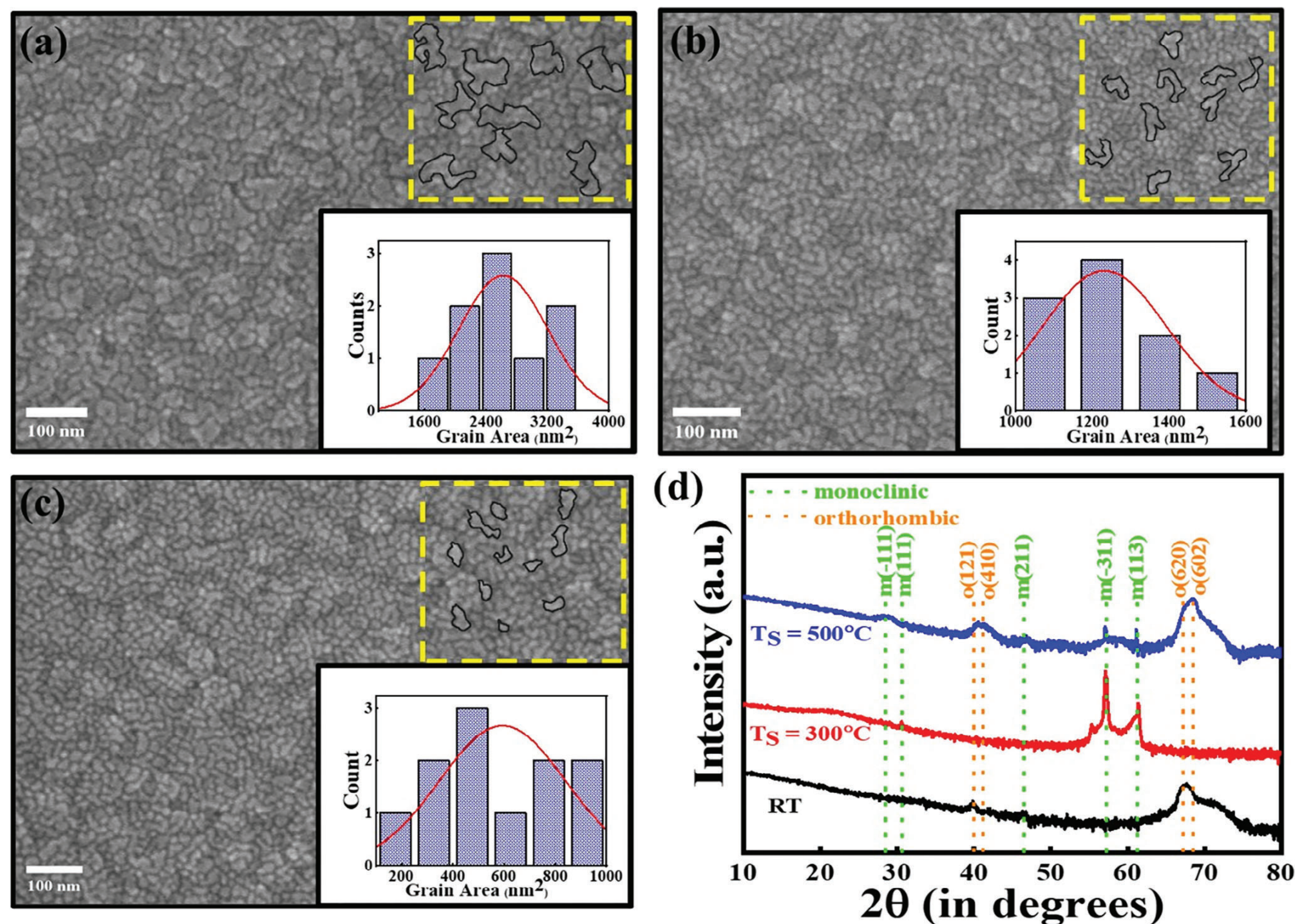

Figure 1. Typical FESEM images of the HfO_2 films a) at RT, and with a substrate temperature of b) 300 °C and c) 500 °C, where the respective grain size distribution is depicted in the inset. (d) The GIXRD patterns of the HfO_2 films grown at RT (black) and with a substrate temperature (T_S) of 300 °C (red) and 500 °C (blue).

Using TEM, Jang et al.[10] further reported the OV-driven electroforming via strong metal interaction. Several other in-situ characterization techniques and device modeling methods, aiming to monitor and analyze the switching behavior of memristors at the single-atom level have also been explored.[22]

Despite numerous studies on RRAM devices, a key question still remains unresolved: precise control over the injection of metal cations and the OV-driven filament formation, while improving electrical performance, especially multilevel behavior for neuromorphic application. The present challenge is to understand the mechanisms involved in controlling the dynamics of CF by exploring the structural, chemical and microstructural properties, and therefore the multilevel behavior in RRAM devices.

In this study, we present a novel strategy that leverages the self-assembled nanochannels in the HfO_2 films for guiding the formation of OV driven CF to ensure a stable and repeatable switching behavior. The optimal performance of RRAM devices is found to be achieved with a stable multilevel behavior by growing the HfO_2 films at 300 °C due to the evolution of maximum OV as evidenced by X-photoelectron spectroscopy (XPS). The phase of the HfO_2 films, determined by grazing incidence X-ray diffraction (GIXRD), is shown to be governed by the substrate temperature, where it achieves a monoclinic phase with highest OV concentration at 300 °C. Moreover, the nanochannels are experimentally evidenced by high-resolution TEM (HRTEM), where the electron energy loss spectroscopy (EELS) mapping reflects the elemental mapping. The formation of the monoclinic phase, coupled with self-assembled nanochannels enables superior multilevel switching behavior with a substantial R_{on}/R_{off} ratio, low operating voltage, and excellent retention and endurance properties. Our findings provide critical insights into the design of highly stable and energy-efficient RRAM devices, positioning them as ideal candidates for future high-density memory and neuromorphic computing applications.

2. Results and Discussion

Figure 1 presents the FESEM images of the surface morphology of HfO_2 films at RT (Figure 1a), 300 °C (Figure 1b), and 500 °C (Figure 1c), showing a significant evolution of grains with increasing substrate temperature. Close inspection reveals the formation of relatively large and irregular grains with a broad size distribution (inset) at RT. However, the average grain size

 © 2024 Wiley-VCH GmbH

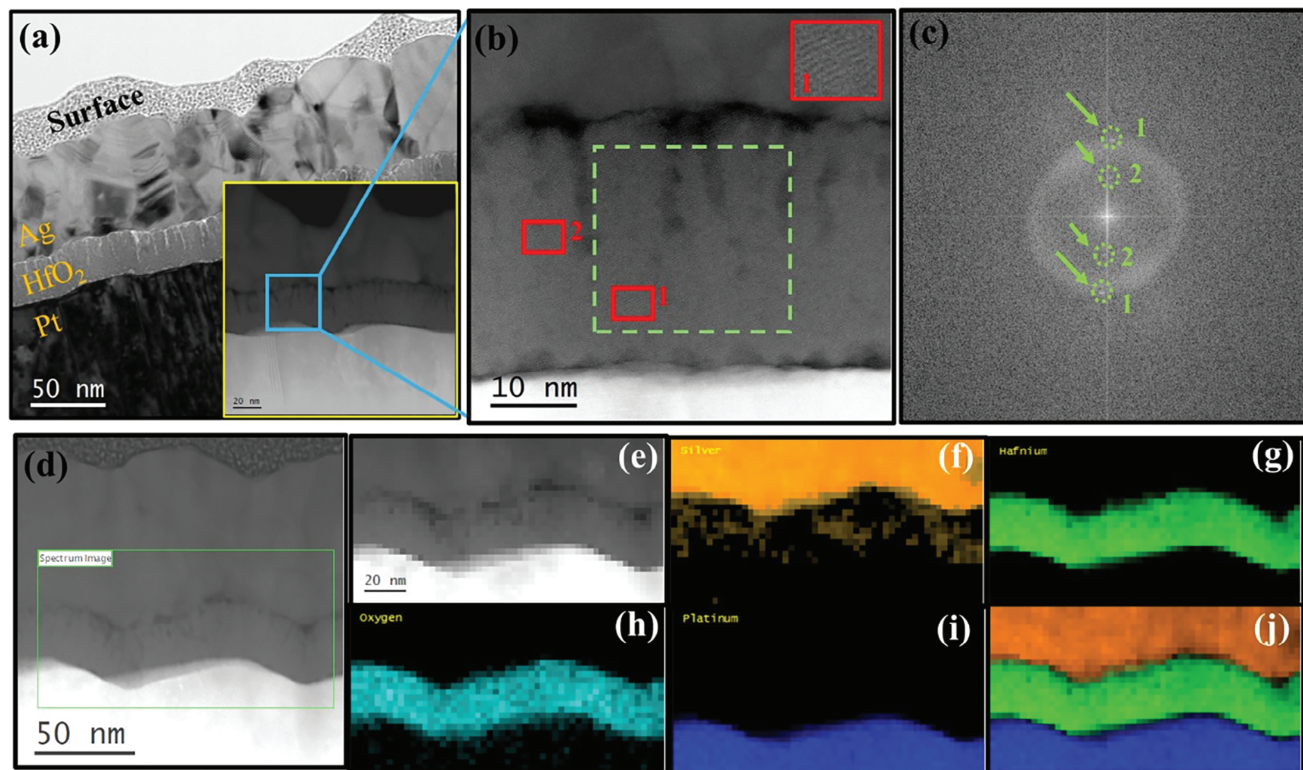

Figure 2. a) The bright field XTEM image of the Ag/HfO_2/Pt device structure, where the inset displays a HAADF STEM image of the active region of the device. b) A magnified HAADF image of the HfO_2 film from the blue box in the inset of a) highlights the presence of nanochannels and the scattered atomic ordering, marked by red boxes, where the closer view of the red box #1 shown in the top-right corner. The FFT analysis of the region marked by the green dashed box in (b) is shown in (c), showing the amorphous ring with superimposed diffraction spots 1 and 2 which are surrounded by the dotted circles. The HAADF image of another region in (d) is used for EELS mappings from the region highlighted by a green box and reflected in (e) for the Ag (f), Hf (g), O (h), and Pt (i) edges along with their overlapping in (j) for clarity.

is found to be gradually reduced and more uniform with elevated substrate temperature at 300 °C and 500 °C. The inset in each FESEM image provides the corresponding grain area distribution histograms, illustrating a clear trend of decreasing grain area in the HfO_2 films with increasing substrate temperature. This is facilitated by the nucleation-driven growth on the substrate, where the growth of the HfO_2 films can be attributed to the ballistic deposition of molecules on initially grown smaller and densely packed grains at elevated temperature with increasing atomic diffusion.[23]

The GIXRD patterns of the HfO_2 films grown at RT and with a substrate temperature (T_S) of 300 °C and 500 °C are exhibited in Figure 1d. The reflections in the GIXRD results suggest the formation of crystalline grains.[24,25] We should note here that the grain boundaries often act as scattering centers for charge carriers and thus can control the charge transport mechanism in HfO_2. Therefore, optimizing the grain size distribution through controlled deposition parameters is crucial for achieving the desired balance between high dielectric constant and low leakage current in HfO_2 films.

The GIXRD analysis of HfO_2 films (see Figure 1d) reveals a distinct phase change with increasing substrate temperature upto 500 °C. Close inspection of the result at RT indicates the formation of local ordering in the disordered HfO_2 film with the orthorhombic phase, showing predominant reflections from the (620) and (602) planes (JCPDF#01-078-5755) on a broad hump. The key finding is the clear transition to thermodynamically stable monoclinic phase with the dominant reflections from the (−311) and (113) planes (JCPDF#01-078-5754) at a substrate temperature of 300 °C. Upon further increase in substrate temperature to 500 °C, the GIXRD result reveals the coexistence of both monoclinic and orthorhombic phases. The GIXRD results therefore demonstrate the important role of the substrate temperature in determining the nucleating phase and the related phase transformation at elevated temperature.

The monoclinic phase, which is dominant at 300 °C and also present at 500 °C, is particularly beneficial for resistive switching applications due to the availability of the highest concentration of OV for having lower symmetry and structural distortion compared to the orthorhombic phase.[26] We should note here that OV play a crucial role in resistive switching by facilitating the formation and rupture of CF, which control the switching between high resistance state (HRS) and low resistance state (LRS). The abundance of OV in the monoclinic phase enhances the formation of stable, well-defined conductive paths, making it the most favorable phase for achieving reliable resistive switching performance.

To evaluate the film crystallinity and microstructure of the device, TEM analysis was performed on the S2 sample, and the results shown in **Figure 2**. The cross-sectional TEM (XTEM)

 © 2024 Wiley-VCH GmbH

16136829, 2025, 7, Downloaded from https://onlinelibrary.wiley.com/doi/10.1002/smll.202409798 by Indian Institute Of Technology, Wiley Online Library on [05/06/2026]. See the Terms and Conditions (https://onlinelibrary.wiley.com/terms-and-conditions) on Wiley Online Library for rules of use; OA articles are governed by the applicable Creative Commons License

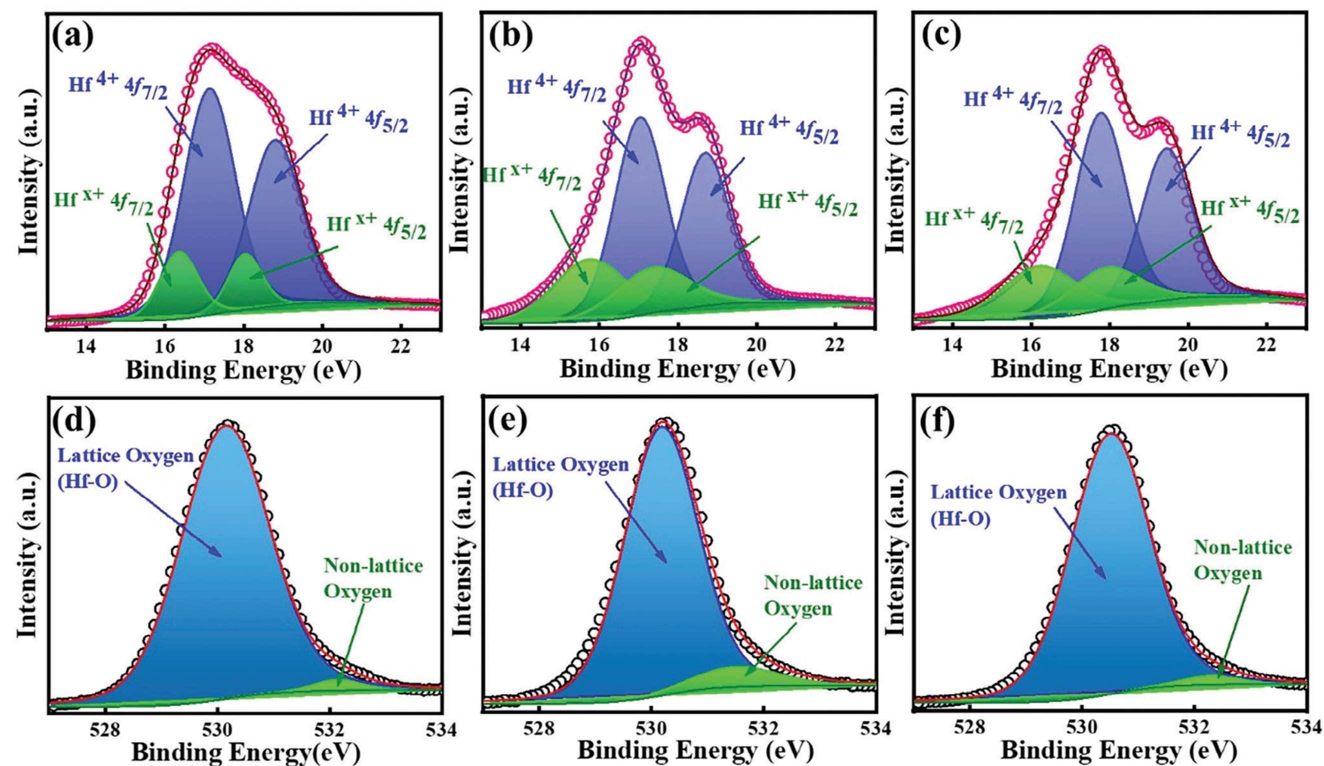

Figure 3. Core level Hf 4*f* spectra of a) S1, b) S2, and c) S3 samples, and core level O 1s spectra of d) S1, e) S2, and f) S3 samples, respectively. The deconvoluted peaks of the respective spectrum are also superimposed on the experimental results for clarity.

image of the Ag/HfO_2/Pt device structure in bright field mode is shown in Figure 2a, revealing the HfO_2 layer thickness to be ≈25 nm with columnar structure. The high angle annular dark field (HAADF) scanning TEM (STEM) image of the same is presented in the inset as well to follow the uniformity of the deposited HfO_2 film. The magnified HAADF STEM image of the Ag/HfO_2/Pt layers from the blue region (inset, Figure 2a) is projected in Figure 2b, showing the formation of self-assembled nanochannels near the surface of the HfO_2 film. It appears to be amorphous in nature with some local atomic ordering within the matrix. The red squares in Figure 2b are highlighting the regions of local crystallinity. A closer view of the red box #1, located in the top-right corner of Figure 2b, shows the crystalline planes in this region.

The observed nanochannels play a crucial role in the formation of guided CF for controlling the resistive switching behavior. Figure 2c presents the Fast Fourier Transform (FFT) image of the green-dashed region in Figure 2b showing the amorphous ring with superimposed diffraction spots 1 and 2 (surrounded by the dotted circles) corresponding to crystalline planes of the HfO_2 film. Another HAADF image is shown in Figure 2d for exploring the elemental distribution within the green region as presented in Figure 2e by EELS mapping at the Ag, Hf, O, and Pt edges in Figure 2f–i. The overlapped EELS mappings for all these edges are displayed in Figure 2j for clearly distinguishing each layer of the Ag/HfO_2/Pt device. A closer look of the EELS mapping at the Ag edge in Figure 2f reveals the diffusion of Ag into the HfO_2 matrix. Interestingly, the Ag is visible near the surface region of the nanochannels and can also participate in the formation of CF by confining their migration between the channels. This in turn prevents the unwanted lateral expansion that could lead to an unstable low resistance state (LRS).

After close inspection of the role of nanochannels and Ag cations, to study the role of OV in the present case, XPS analysis of S1, S2, and S3 films has been carried out in a systematic way. This analysis also provided insight into the chemical composition of the films, with the results shown in **Figure 3a–f**.

XPS survey scans were recorded for all S1, S2, and S3 samples before sputtering (see upper panel of Fig S1 (a-c)), where all the spectra were calibrated using the C 1*s* peak at 284.08 eV and analyzed using the CasaXPS software. After calibration of C 1*s* peak, the samples were sputter cleaned to remove any possible contamination on the surface, and again, the survey scan was recorded (see lower panel of Figure S1d–f, Supporting Information) prior to high-resolution XPS (HRXPS) studies. The HRXPS results of the Hf 4*f* and O 1*s* core level of the respective samples are presented in Figure 3a–f. These peaks are deconvoluted by applying the Voigt (70% Gaussian + 30% Lorentzian) function after subtracting the Shirley background correction for detailed analysis. The deconvoluted peaks of the respective spectrum are also superimposed on the experimental results to follow the impact on the chemical properties of the HfO_2 films with increasing substrate temperature up to 500 °C. In fact, we aimed to engineer defect concentrations, specifically OV, by adjusting the substrate temperature for optimizing the resistive switching behavior. The calculated full width at half maximum (FWHM), peak positions, and atomic percentages (at.%) are summarized in **Tables 1–3** for clarity.

 © 2024 Wiley-VCH GmbH

16136829, 2025, 7, Downloaded from https://onlinelibrary.wiley.com/doi/10.1002/smll.202409798 by Indian Institute Of Technology, Wiley Online Library on [05/06/2026]. See the Terms and Conditions (https://onlinelibrary.wiley.com/terms-and-conditions) on Wiley Online Library for rules of use; OA articles are governed by the applicable Creative Commons License

Table 1. Fitting components like FWHM, peak position, and at.% for the Hf 4*f* and O 1s levels of S1 sample.

S1 sample	Hf^{4+} $4f_{7/2}$	Hf^{4+} $4f_{5/2}$	Hf^{x+} $4f_{7/2}$	Hf^{x+} $4f_{5/2}$	O 1s [LO]	O 1s (NLO)
FWHM (eV)	1.55	1.58	1.14	1.02	1.87	0.97
Peak position (eV)	17.13	18.80	16.36	18.04	530.14	532.15
at.%	46.94	35.17	10.25	7.65	98.08	1.92

Table 2. Fitting components like FWHM, peak position, and at.% for the Hf 4*f* and O 1s levels of S2 sample.

S2 sample	Hf^{4+} $4f_{7/2}$	Hf^{4+} $4f_{5/2}$	Hf^{x+} $4f_{7/2}$	Hf^{x+} $4f_{5/2}$	O 1s [LO]	O 1s (NLO)
FWHM (eV)	1.52	1.47	2.15	2.22	1.56	1.79
Peak position (eV)	17.54	19.20	16.25	17.87	530.67	532
at.%	39.62	29.62	17.51	13.14	92.29	7.71

Figure 3a–c displays the XPS spectra of the Hf 4*f* core level for the S1, S2, and S3 films. The Hf $4f_{7/2}$ and Hf $4f_{5/2}$ doublets of the Hf 4*f* level for each sample are deconvoluted into four distinct peaks. For S1, the peaks at 16.36 and 18.04 eV correspond to the Hf $4f_{7/2}$ and Hf $4f_{5/2}$ states of oxygen-deficient HfO_2, while the peaks originated at 17.13 and 18.80 eV are attributed to stoichiometric HfO_2.[27,28] In S2, the Hf $4f_{7/2}$ and Hf $4f_{5/2}$ peaks at 16.25 and 17.87 eV indicate oxygen-deficient HfO_2, with stoichiometric peaks at 17.54 and 19.20 eV. The increased area of the oxygen-deficient peaks in S2 compared to S1 suggests a higher concentration of OV, further supported by the O 1*s* spectra in Figure 3d,e. Due to the asymmetric shape of the O 1*s* spectra, they were also deconvoluted into two peaks centered at ≈530.14 and 532.15 eV for S1 and at 530.67 and 532 eV for S2. Higher B.E. peak is assigned to non-lattice oxygen (NLO) in oxygen-deficient regions, while the lower B.E. peak corresponds to lattice oxygen (LO).[27–29]

For sample S3, the oxygen-deficient Hf $4f_{7/2}$ and Hf $4f_{5/2}$ peaks are found to be at ≈16.22 and 17.89 eV, and the stoichiometric peaks are at 17.76 and 19.49 eV. Interestingly, the area of oxygen-deficient peaks in S3 decreases compared to S2, indicating that S2 has the highest concentration of OV, which aligns with its monoclinic phase (see Figure 1d). This observation is consistent with previous studies,[26] showing that the monoclinic phase tends to accommodate more OV due to its stable and symmetrical geometry compared to the orthorhombic phase. This is further supported by Figure 3f, where the non-lattice O 1*s* peak at 532.79 eV gives a marked reduction in at.% with respect to the lattice O 1*s* peak at ≈531 eV. From Tables 1–3, the 98.08 at.% of LO in S1 is found to be dropped to 92.29 at.% for S2, but further increased to 97.69 at.% for S3, confirming the highest concentration of OV in S2. This is also reflected from the corresponding at.% of the NLO peak for S1, S2, and S2.

Typically, OV (defects in the crystal structure, where oxygen atoms are absent from their lattice sites) are generated at grain boundaries, and as the average grain size decreases, the grain boundary area increases.[30,31] As revealed from our XPS analysis, the concentration of OV is strongly affected by the growth temperature of the HfO_2 layer, where the increase in substrate temperature enhances oxygen mobility and promote the formation of OV via thermal activation. Consequently, the concentration of OV in the film grown at 300 °C (S2) rises as compared to S1. The high OV concentration in S2 is associated with a phase transformation from orthorhombic to monoclinic (see Figure 1d).[26,31] However, the average grain size in the monoclinic phase is nearly an order of magnitude larger than in the orthorhombic phase, which explains the coexistence of both monoclinic and orthorhombic phases in S3, and the corresponding reduction in OV concentration. Therefore, in this case, both OV concentration and average grain size play a critical role in phase transformation from orthorhombic to monoclinic.

To check the performance of these HfO_2 films, the current-voltage (*I*–*V*) characteristics of the Ag/HfO_2/Pt device structures were investigated by sweeping the applied voltage on the Ag electrode from −0.3 V→0 V→+0.3V→0 V as the one shown in **Figure 4a**.

As discerned from Figure 4a, the steady increase in positive voltage on the device from 0 V to a certain positive voltage changes the device from HRS to LRS, called the "SET" process, whereas it changes from LRS to HRS in the "RESET" process by imposing the voltage from 0 V to a negative voltage. Interestingly, no electroforming process is found in this RS process without using a compliance current, which is often needed during the SET process to prevent excessive current that could damage the device or affect its reliability.

Table 3. Fitting components like FWHM, peak position, and at.% for the Hf 4*f* and O 1s levels of S3 sample.

S3 sample	Hf^{4+} $4f_{7/2}$	Hf^{4+} $4f_{5/2}$	Hf^{x+} $4f_{7/2}$	Hf^{x+} $4f_{5/2}$	O 1s [LO]	O 1s (NLO)
FWHM (eV)	1.55	1.52	2.21	2.09	1.65	1.2
Peak position (eV)	17.76	19.49	16.22	17.89	531	532.79
at.%	41.5	31.27	15.56	11.66	97.69	2.31

© 2024 Wiley-VCH GmbH

16136829, 2025, 7, Downloaded from https://onlinelibrary.wiley.com/doi/10.1002/smll.202409798 by Indian Institute Of Technology, Wiley Online Library on [05/06/2026]. See the Terms and Conditions (https://onlinelibrary.wiley.com/terms-and-conditions) on Wiley Online Library for rules of use; OA articles are governed by the applicable Creative Commons License

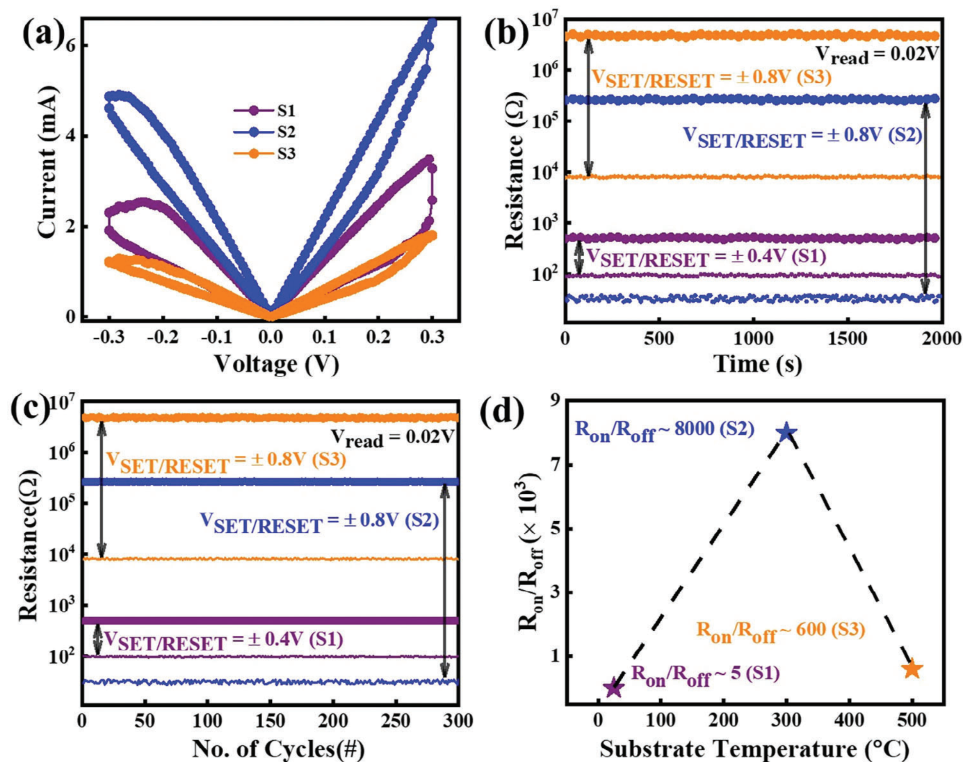

Figure 4. a) Resistive switching characteristics (*I–V* curves), b) retention test, c) endurance test, and d) R_{on}/R_{off} ratio focomparison of devices using S1, S2, and S3 samples. The HRS and LRS in (b,c) are marked by thick and thin lines, respectively.

When the same potential bias is applied to all devices, distinct differences are observed in their respective *I-V* characteristics. As shown in Figure 4a, the current values are highest for the S2 sample, followed by S1, with S3 exhibiting the lowest current. This can be attributed to the uniform grain growth and the stable monoclinic phase present in the S2 sample, which enhances the formation of CF with improved current conduction mechanism. In contrast, the S1 and S3 samples show less distinct switching, likely due to the variations in grain structure and phase composition, with S3, which has smaller grains and mixed phases, displaying the least efficient switching characteristics.

To further investigate the reliability of the devices, both retention and endurance properties were evaluated, as shown in Figure 4. In fact, the typical DC retention data recorded up to 2000 sec with a read voltage of V_{read} = 0.02 V at RT is shown in Figure 4b. It is evident that the S1 device gives a small gap between the HRS and LRS, resulting in a low R_{on}/R_{off} ratio. In contrast, the S2 device exhibits a more pronounced separation, with the HRS shifting to higher resistance and the LRS shifting to lower resistance, leading to a significantly improved R_{on}/R_{off} ratio. Surprisingly, instead of following this trend, the S3 device shows both LRS and HRS shifting to higher resistance, which counterintuitively results in a lower on/off ratio compared to S2.

To assess the repeatability of the resistive switching behavior in these RRAM devices, endurance tests were performed. Figure 4c displays the DC endurance results after 300 switching cycles for all devices. A similar trend is observed in the retention test, with S2 demonstrating the best endurance performance, while S1 and S3 exhibit less stable behavior, further highlighting the superior switching characteristics of the S2 device.

The R_{on}/R_{off} ratios for the S1, S2, and S3 samples are estimated to be 5, 8000, and 600, respectively, as shown in Figure 4d. As discerned, the S2 sample exhibits the highest R_{on}/R_{off} ratio, which can be attributed to its superior grain growth and the formation of a more stable monoclinic phase (discussed above). This phase is associated with a higher concentration of OV,[26] which enhances the resistive switching behavior, resulting in a significantly improved R_{on}/R_{off} ratio compared to S1 and S3.

To investigate the multi-level switching behavior of the devices, *I–V* cycles were performed with varying stop voltages during RESET operation. The device with S2 has shown the highest number of distinct HRS with respect to S3 and S1, confirming the better multilevel behavior as the one shown in **Figure 5a** in the presence of highest OV concentration (see Figure 3). The multilevel behaviors of S3 and S1 devices have also been illustrated in Figure S2 (Supporting Information) for clarity.

I–V curves for multiple HRS states have been replotted in the high field region (V > 0.3 V) as ln(I) versus $V^{1/2}$ on a logarithmic scale (see Figure 5b). The linearly fitted trend observed in the ln(I) versus $V^{1/2}$ pots indicates that the dominant conduction mechanism is thermionic emission, as described by [1,7]

$$J = A^{*}\, T^{2} \exp\left(\frac{-q\left(\varphi_B - \sqrt{\frac{qV}{4\pi\varepsilon d}}\right)}{kT} \right) \tag{1}$$

 © 2024 Wiley-VCH GmbH

16136829, 2025, 7, Downloaded from https://onlinelibrary.wiley.com/doi/10.1002/smll.202409798 by Indian Institute Of Technology, Wiley Online Library on [05/06/2026]. See the Terms and Conditions (https://onlinelibrary.wiley.com/terms-and-conditions) on Wiley Online Library for rules of use; OA articles are governed by the applicable Creative Commons License

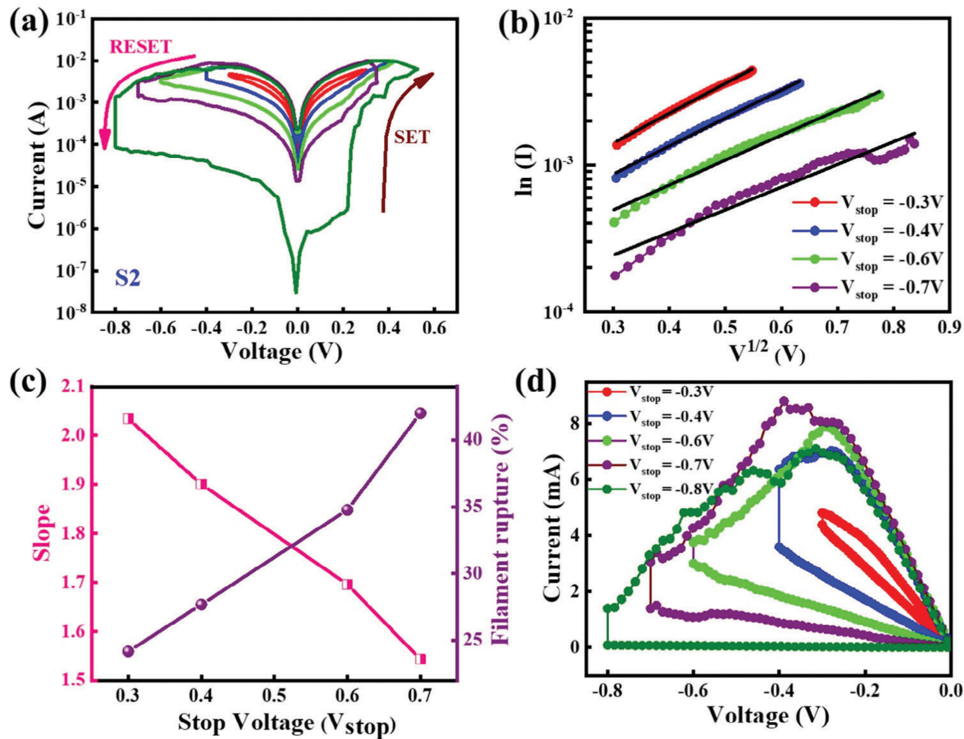

Figure 5. a) RESET voltage-dependent multi-level *I–V* resistive switching characteristics of the S2 device. b) Richardson plots (ln(I) vs $\sqrt{V}$) analysis of the HRS states of stop voltage-based multilevel states. c) Extracted slope values from the Richardson plots and filament rupture percentage for different stop voltages in V. d) DC *I–V* characteristic curve of the device during gradually increasing stop voltage during the RESET process.

where A^* is the effective Richardson constant, φ_B is the barrier height, ε is the dielectric permittivity, k is the Boltzmann constant, T is the temperature, and d represents the rupture length of the filament. By taking the logarithm of Equation (1), the relationship between the intercept and slope can be expressed as

$$slope \propto \sqrt{\frac{1}{d}} \tag{2}$$

Figure 5c displays the slope values obtained from Equation (2) across different reset voltages. As the RESET-stop voltage increases from 0.3 to 0.7 V, the slope of the device decreases from 2.03 ± 0.01 to 1.54 ± 0.01 (see Figure 5c, left *y*-axis). A reduced slope in the ln(I) versus $V^{1/2}$ plots indicates a larger d value, according to Equation (2). This observation can be interpreted as an increased filament rupture length, as shown on the right *y*-axis of Figure 5c. Consequently, higher RESET-stop voltages lead to elevated HRS states. Importantly, our experimental findings on the variation of filament rupture length with RESET-stop voltages are consistent with previously reported simulation models, such as the Stanford/ASU Model[32] and the Huang Physical Model.[33] Figure 5d illustrates the gradual reset process of the S2 device under different stop voltages. While the LRS remains nearly the same across the various stop voltages, distinct HRS levels are clearly observed. This indicates that the HRS can be effectively modulated by adjusting the stop voltages.

The stability of different HRS was also confirmed by endurance tests for 300 cycles in each V_{stop} (see **Figure 6**a). As can be seen, the LRS, along with multiple HRS, is obtained from the RESET *I-V* characteristics for a read voltage of 0.02 V. The average resistance states are found to be ≈69.4, 119, 229, 573.3, and 264.5 kΩ for HRS with RESET voltages of −0.3, −0.4, −0.6, −0.7, and −0.8 V, respectively. Data retention is also an important property for different HRS stabilities and synaptic applications. Figure 6b shows the retention properties up to 1500 sec for distinct LRS and five different HRS for testing the reliability of multi-state resistance.

Additionally, Figure 6c presents the cumulative probability plots for the LRS and multiple HRS states at different stop voltages, demonstrating uniform resistance distribution across all states. Figure 6d shows a clear trend of increasing average HRS resistance as the RESET stop voltage is raised.

All these findings demonstrate that our device is highly capable of multilevel operation, achieving an impressive R_{on}/R_{off} ratio of 8000 and retention of each HRS for up to 1500 sec. Additionally, the device exhibits an excellent memory window, and maintains a stable LRS and five distinct HRS with minimum fluctuations. A key advantage of our device is its lower operating voltage, with significantly reduced SET/RESET voltages compared to the existing devices. Moreover, it operates as a forming-free device, eliminating the need for an initial forming process. It does not require the application of a compliance current, simplifying its operation and enhancing reliability. To evaluate device performance, multiple RRAM devices were

© 2024 Wiley-VCH GmbH

16136829, 2025, 7, Downloaded from https://onlinelibrary.wiley.com/doi/10.1002/smll.202409798 by Indian Institute Of Technology, Wiley Online Library on [05/06/2026]. See the Terms and Conditions (https://onlinelibrary.wiley.com/terms-and-conditions) on Wiley Online Library for rules of use; OA articles are governed by the applicable Creative Commons License

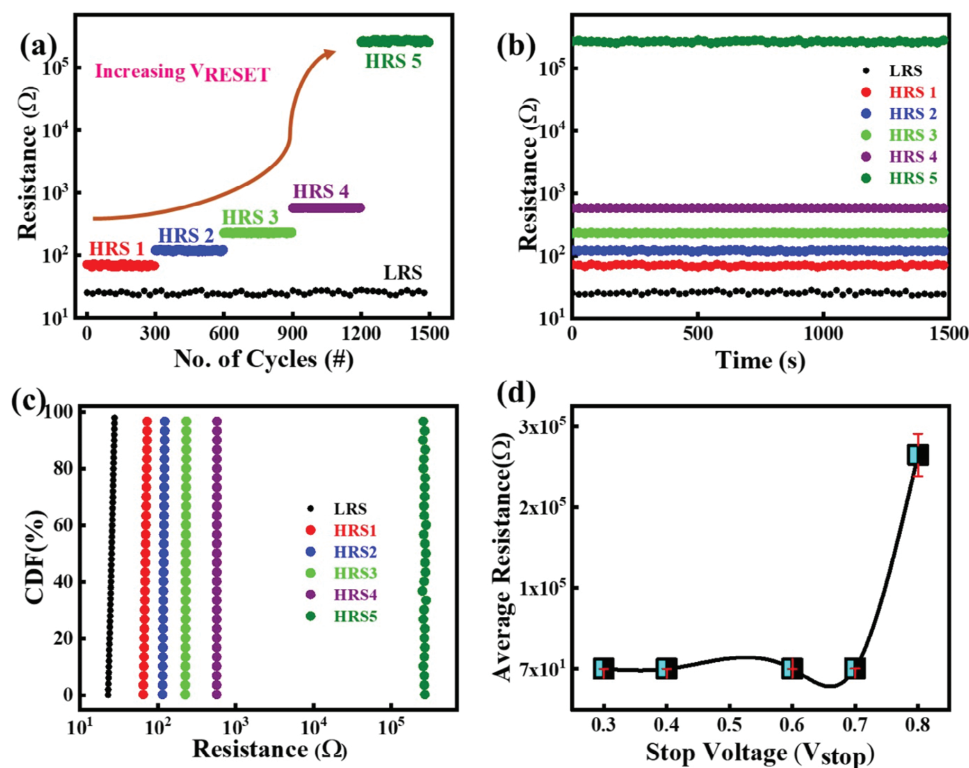

Figure 6. a) Endurance properties, b) retention test, c) the cumulative probability distribution of the LRS and for different HRS states for the multi-level states achieved by varying stop voltages. d) Variation of average resistance during HRS with increasing stop voltages in V.

tested both within the same batch and across different fabrication batches. The results demonstrated consistent performance, confirming high reproducibility across devices. A comparison with previously reported devices featuring similar configurations and structures further highlights these advantages, such as higher R_{on}/R_{off} ratios, lower operating voltages, improved retention times, and superior stability in both LRS and HRS states. These attributes confirm superior resistive switching behavior of our device, making it a strong candidate for advanced memory applications. A comparison table follows further to illustrate its performance superiority over previously published results.

As evident from the comparison, devices with large operating windows often suffer from poor retention of intermediate states and higher power consumption. On the other hand, devices with strong retention and low power consumption typically demonstrate limited operating windows and lack precise linear control. In contrast, the findings reported here mark a significant advancement, offering both low-power operation and reliable retention, alongside a wide and well-controlled operating window. This makes our device highly suitable for low-power neuromorphic applications and multi-bit storage, addressing key limitations seen in previous works.

By considering all the experimental results here, we propose a comprehensive model, as illustrated in **Figure 7**. It shows the formation of CF at LRS and their gradual rupture for achieving distinct HRS.

Additionally, the HAADF STEM images are presented, showing the presence of self-assembled nanochannels, while EELS mapping provides further validation, linking the proposed model to the experimental evidence. XPS analysis reveals a sufficient concentration of OV that contributes to the formation of CF, playing a critical role in switching dynamics. HAADF images further confirm the presence of multiple nanochannels near the TE, a finding supported by EELS mapping at Ag edge, which shows some diffusion of Ag into the matrix at their interfaces. However, a detailed comparison between the HAADF images and EELS mapping reveals an intriguing phenomenon: Ag cation diffusion occurs primarily in areas where nanochannels are absent, suggesting that Ag cations are confined to a sub-nanoscale regime, guiding the formation of CF within the matrix. These guided filaments, comprising both Ag cations and OV, form a stable conductive pathway. These defined conducting pathways upon application of varying stop voltage, provide a better control over dissolution of CF, thus enabling a stable and robust multilevel behavior.

Evidence from the EELS mapping shows that Ag cation diffusion spans only a few nanometers, indicating that multi-level switching is largely governed by the controlled introduction of OV into the monoclinic HfO_2 matrix, achieved through substrate temperature optimization during oxide layer growth. The formation of nanochannels at the interface facilitates the creation of well-defined and guided CF rather than random paths that lead to fluctuations in the LRS. As a result, the LRS is highly stable, with a well-defined and consistent conductive path.

When a positive bias is applied to TE, Ag cations migrate through the nanochannel boundaries, forming CF. Simultaneously, oxygen ions from NLO in the HfO_2 layer migrate toward TE, creating additional OV that join the pre-existing

© 2024 Wiley-VCH GmbH

16136829, 2025, 7, Downloaded from https://onlinelibrary.wiley.com/doi/10.1002/smll.202409798 by Indian Institute Of Technology, Wiley Online Library on [05/06/2026]. See the Terms and Conditions (https://onlinelibrary.wiley.com/terms-and-conditions) on Wiley Online Library for rules of use; OA articles are governed by the applicable Creative Commons License

16136829, 2025, 7, Downloaded from https://onlinelibrary.wiley.com/doi/10.1002/smll.202409798 by Indian Institute Of Technology, Wiley Online Library on [05/06/2026]. See the Terms and Conditions (https://onlinelibrary.wiley.com/terms-and-conditions) on Wiley Online Library for rules of use; OA articles are governed by the applicable Creative Commons License

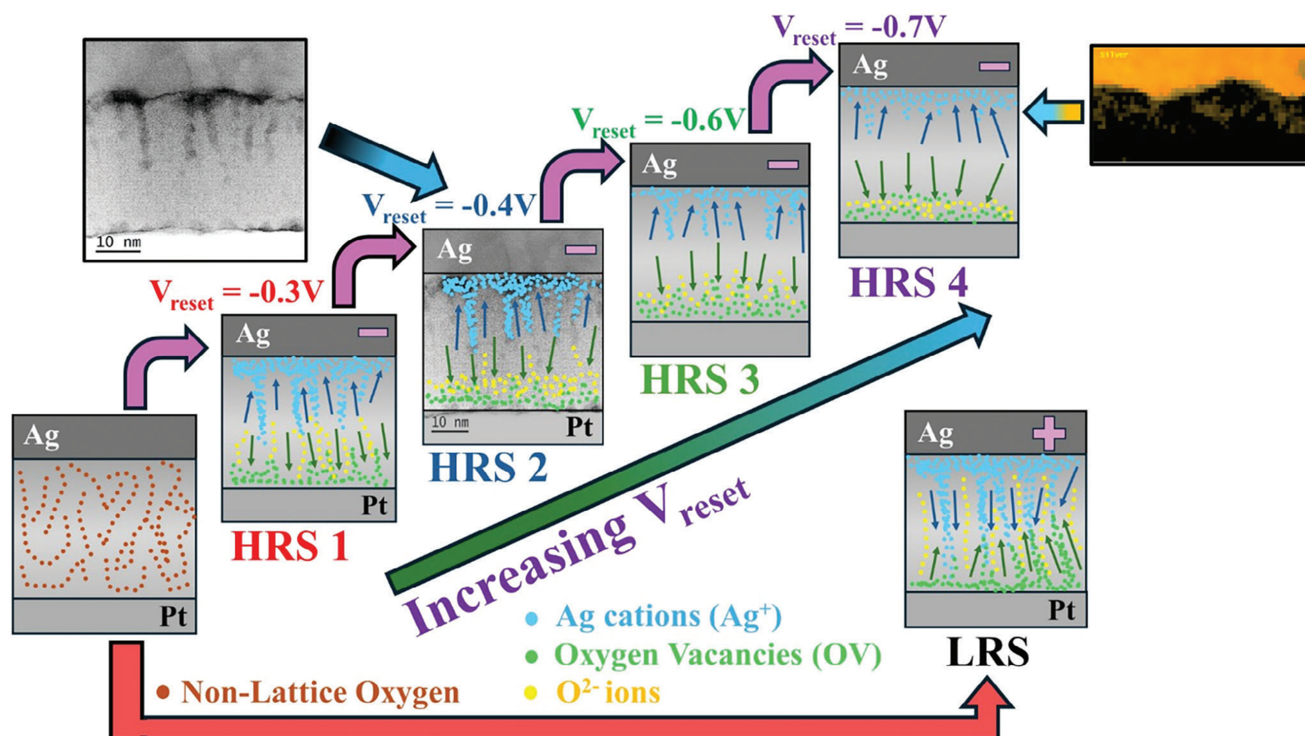

Figure 7. The proposed model for the resistive switching mechanism of the Ag/HfO_2/Pt device, based on the evidence from HAADF STEM images and EELS mapping.

ones, ultimately connecting to the cationic filament along the nanochannel boundaries. This dual ionic filament switches the device to a stable LRS. When a negative potential is applied, Ag cations migrate back to TE, and oxygen ions recombine with the OV, breaking the CF and transitioning the device to an HRS. With increasing stop voltage, this CF rupture occurs in steps, leading to multiple distinct HRS levels.

By varying the applied stop voltages, we successfully achieved stable multiple HRS levels and a single LRS, enabled by the well-defined and guided conductive paths formed by nanochannels at the interfaces. This ensures stable switching states and enhances the device repeatability, consistently forming CF at the same locations.

To gain insight into the intrinsic memristive mechanisms of the RRAM devices, the impedance (i.e., $Z = Z' + jZ''$ consisting of real (Z') and imaginary (Z'') parts) spectroscopy measurements for S2 device have also been conducted by frequency domain analysis, and the results are presented in **Figure 8**.

Figure 8a shows the complex plane plot (Nyquist diagram) of S2 device taken at RT, in which the *x*-axis is the real part, and the *y*-axis is the negative imaginary part. The truncated semicircle observed in the Nyquist plot indicates the presence of both bulk and interface phenomena influencing the impedance response of the device. A single semicircle can be found in the Nyquist graph of the recorded impedance spectra with an offset on the real axis (Figure 6a). This hints toward the existence of a single RC element for the equivalent circuit for the stationary voltage region. Since the Nyquist curves do not pass through the origin, it can be assumed that the associated equivalent circuit must be an arrangement of two resistors and one capacitor.[3,42,43]

The high-frequency end of the Nyquist plot represents the bulk properties of the HfO_2 thin film. The presence of a semicircular arc in this region suggests a parallel combination of a resistor and a capacitor, indicative of charge transport through the bulk material. The low-frequency tail of the Nyquist plot, where the semicircle appears truncated, is typically associated with interfacial phenomena.[3,42,43] This truncation suggests the presence of additional resistive components, likely due to charge transfer resistance at the HfO_2/Pt interfaces. An equivalent circuit model was used to quantitatively analyze the impedance data. The model, depicted in Figure 8d, consists of a parallel RC circuit representing the bulk properties and a series resistor accounting for the interface resistance. The fitting parameters obtained from this model provide the bulk resistance (R_P) and capacitance (C_P), as well as the interface resistance (R_S) are given in **Table 4**.

From the obtained parameters, it is clear that both the bulk HfO_2 and interface contact resistances are lowest when the device is unbiased. When subjected to a DC bias of 100 mV and 200 mV, the interface resistance increased to 43.32 and 46.42 Ω in the HRS, respectively, with corresponding increases in bulk resistance. This suggests an expanded switching window, confirming multi-level switching behavior. Additionally, the bulk capacitance values decreased with increasing voltage bias, indicating the device's ability to achieve tunable resistance and capacitance states under varying voltage conditions.

The Bode plots in Figure 8b provide further insight into the phase angle (ϕ) and impedance magnitude ($|Z|$) across different frequencies for each state. Without bias, the plot shows a high $|Z|$ at lower frequencies, reflecting significant resistance to charge transport. The $|Z|$ however drops by applying DC

 © 2024 Wiley-VCH GmbH

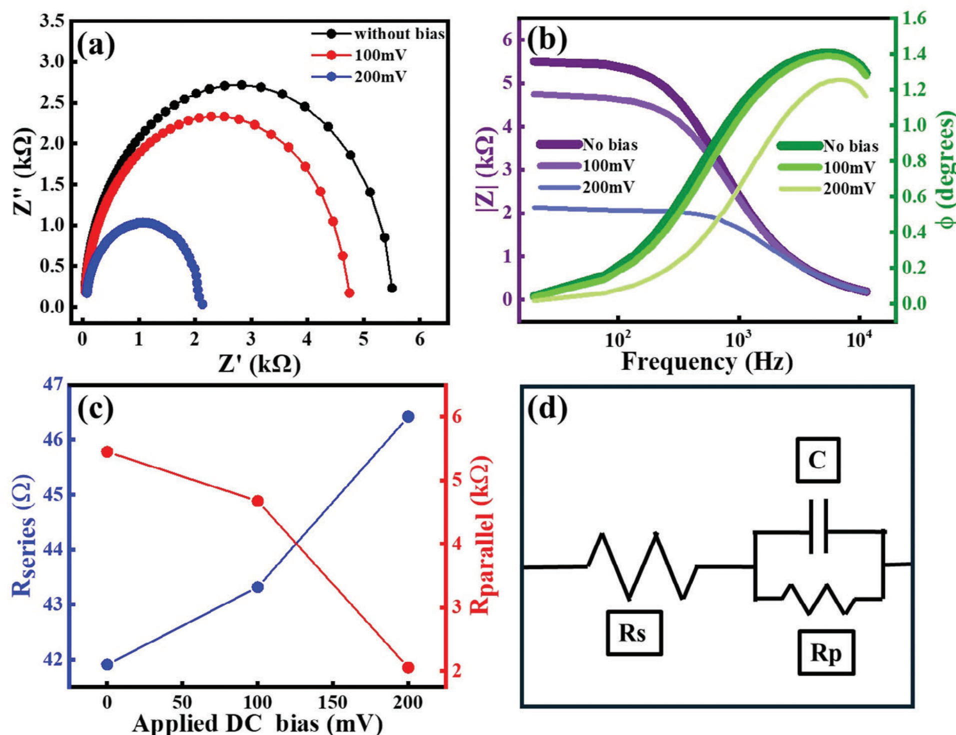

Figure 8. a) Nyquist plots of the data for varying DC voltages on the S2 device. b) the Bode plots show the change in impedance modulus |Z| and phase angle (ϕ) with varying frequency for the S2 device without and with bias of varying magnitude. c) Variation of obtained parallel and series resistance values with applied DC bias. d) Equivalent circuit for fitting the obtained datasets.

voltages of 100 and 200 mV, consistent with the formation of CF within the HfO_2 layer. Phase angle analysis further reveals the capacitive and resistive contributions to the total impedance. In the unbiased and 100 mV bias states, higher capacitive behavior indicates the charge storage property at the interface, while at 200 mV bias, the reduced capacitive response with increased resistive contribution suggests an increase in charge transport through CF.

The results of this study demonstrate the strong potential of our Ag/HfO_2/Pt-based RRAM devices for advanced resistive switching applications, particularly for multilevel data storage and neuromorphic computing. By precisely controlling the substrate temperature during deposition, we were able to fine-tune the film's microstructure, phase composition, and defect density, leading to enhanced resistive switching performance. The device exhibits a wide switching window with stable, distinct intermediate states and excellent endurance, making it an ideal candidate for multi-bit memory storage. The increased OV concentration and the formation of well-defined CF provide key insights into the underlying switching mechanism. The device's tunable interface and bulk resistances, along with its capacitive behavior under different voltage biases, further highlight its adaptability for low-power applications.

Additionally, the device operates at low voltage, is forming-free, and does not require compliance current, resulting in high energy efficiency and reliability. With a significant R_{on}/R_{off} ratio, stable performance of HRS and LRS over extensive endurance cycles for long retention time, this device outperforms many existing RRAM systems, as shown in the comparative analysis (see Table 5). These qualities make it a robust and scalable solution for next-generation memory technologies as appearing from **Table 5**.

3. Conclusion

In summary, we successfully demonstrated the fabrication of Ag/HfO_2/Pt-based RRAM device with controlled deposition of HfO_2 films by RF magnetron sputtering technique at elevated substrate temperature for achieving stable monoclinic phase with optimized OV as revealed by XPS. In particular, we showed a clear transition to monoclinic phase by utilising a substrate temperature of 300 °C during HfO_2 film deposition. Microstructure

Table 4. Fitting parameters like R_S, R_P, and C_P determined from the equivalent circuit of the Z′ Vs. Z″ (Nyquist) plots of S2 device without bias as well as with DC biases of 100 and 200 mV.

Obtained Parameters	Without bias	With 100 mV bias	With 200 mV bias
Series Resistance (R_S) in Ohm	41.91	43.32	46.42
Parallel Resistance (R_P) in Ohm	6.0043E-8	6.0261E-8	6.1229E-8
Capacitance (C_P) in nF	5449	4674	2056

 © 2024 Wiley-VCH GmbH

16136829, 2025, 7, Downloaded from https://onlinelibrary.wiley.com/doi/10.1002/smll.202409798 by Indian Institute Of Technology, Wiley Online Library on [05/06/2026]. See the Terms and Conditions (https://onlinelibrary.wiley.com/terms-and-conditions) on Wiley Online Library for rules of use; OA articles are governed by the applicable Creative Commons License

Table 5. Comparison of the performances of HfO_x-based devices considering the most used figures of merit.

Device structure [TE/active layer/BE]	Forming potential	V_{set}	V_{reset}	Deposition parameters	Oxygen Vacancy Analysis	R_{on}/R_{off} ratio	Multilevel	Refs.
TiN/HfO_x/Pt	No	1.03 V	−2.7 V	Sputtering, 300 °C	XPS, FESEM Impedance analysis at low temp	≈100	No	[3]
ITO/HfO_x/TiN	5.5–6 V	5 V	−4 V	ALD, 300 °C	NA	NA	No	[34]
TiN/HfO_2/Pt	NA	6 V	−2 V	Sputtering	NA	10^6	Yes	[8]
In/HfO_2/Pt	8.5 V	8 V	−8 V	RF Magnetron Sputtering @ 550 °C T_S	XRD	NA	No	[35]
Pt/HfO_2/Ti/TiN	2 V	1 V	−0.7 V	ALD, 200 °C	NA	10^3	Yes	[36]
Au/HfO_x/HfO_2/Pt	2.5 V	0.3 V	−0.2 V	RF Magnetron Sputtering	XPS	NA	NA	[37]
Pt/HfO_x/Pt	2.2 V	2.5 V to 0.9 V	−0.6 V to −0.9 V	RF Magnetron Sputtering	TEM, AFM	NA	NA	[38]
Ti/HfO_x/Pt	3.18 V	0.6 V	−0.6 V	Reactive Sputtering	TEM, XPS	NA	Yes	[39]
TiN/HfO_2/Ti/TiN	2.5 V	0.7 V	−0.8 V	ALD	NA	2	Yes	[40]
W/HfO_{2-x}/Pt	No	4 V	−3.5 V	RF Magnetron Sputtering	XPS depth profiling	>100	Yes	[11]
W/HfO_2/TiN	Yes	3.5 V	−3.6 V	ALD	AES	NA	Yes	[41]
Ag/HfO_2/Pt	No	0.2 V	−0.2 V	RF Magnetron Sputtering	XPS, TEM, Impedance Spectroscopy	8000	Yes	This work

analysis of Ag/HfO_2/Pt device further confirmed the formation of self-assembled nanochannels near the surface of HfO_2 films where the associated EELS mapping revealed the diffusion of Ag cations at their boundaries. These results collectively support the combined effects of OV and Ag cations in controlling the formation and dissolution of CF by changing polarities of the applied voltage and in turn, provides resistive switching behavior at a low voltage (≈0.2 V) without requiring a forming potential and/or compliance current, offering a substantial R_{on}/R_{off} ratio with reasonable retention and endurance properties. Finally, the synergistic effect of Ag cations and OV along the self-assembled nanochannels was shown to govern the pathway of CF during RESET operation. These characteristics make it an outstanding candidate for multi-bit memory storage and neuromorphic computing, paving the way for the development of scalable, energy-efficient memory technologies.

4. Experimental Section

About 25 nm thick HfO_2 films were deposited on chemically cleaned (area 1 × 1 cm^2) Pt/Ti/SiO_2/Si substrates by radio frequency (RF) magnetron sputtering with a constant power of 80 W for 40 min using a 99.99% pure HfO_2 target (2-inch diameter and 3 mm thick) from Semiconductor wafer. During RF deposition, argon (Ar) gas was purged into the vacuum chamber (base pressure ≈2×10^{-7} Torr) at a flow rate of 40 sccm by maintaining a working pressure of ≈6×10^{-3} Torr. Three sets of samples were prepared by growing the uniform HfO_2 films at room temperature (RT)/without giving substrate temperature (S1), 300 °C (S2), and 500 °C (S3) by rotating the substrate at 6 rpm. The film thicknesses were measured with a stylus Surface Profilometer (Bruker DektakXT) and further validated by a variable angle spectroscopic ellipsometer (J.A. Woollam WVASE32).

The structure of the deposited HfO_2 films was initially examined by lab-scale XRD (Bruker, D8- Discover) with Cu-K_α radiation (wavelength ≈0.154 nm) in the 2θ range of 10°–80° at a grazing incidence angle of 0.8°, where θ is the Bragg angle. The surface morphology of the HfO_2 films was characterized by field emission scanning electron microscopy (FE-SEM) from Jeol (JEM-7001F) in plan-view geometry. The chemical composition of the HfO_2 films was further examined by XPS in an ultrahigh vacuum chamber (≈10^{-9} Torr) with Al-K_α radiation (energy ≈1486.6 eV) from a monochromatic source, where the photoelectrons were investigated by a hemispherical electron analyzer (Thermo Fisher, USA). The sample surfaces were sputter-cleaned in situ by 1 keV Ar^+ ions to remove any surface contaminants before data acquisition. All the spectra were collected in normal emission geometry, where the binding energy (B.E.) scale was calibrated from the Fermi level (E_F) of a gold foil. A charge neutralizer gun was also employed during data acquisition. The microstructures were further investigated by TEM in cross-sectional geometry in a probe-corrected JEOL ARM 200F microscope with an accelerating voltage of 200 kV, where the EELS was used for elemental analysis.

About 100 nm thick disc-like Ag electrodes (diameter ≈100 μm) were deposited on the HfO_2 layers through a shadow mask by thermal evaporation. The HfO_2 film served as an active layer, where Ag and Pt were the top electrode (TE) and bottom electrode (BE), respectively. In this work, two-terminal Ag/HfO_2/Pt RRAM devices were examined by Keithley-4200 semiconductor characterization system and/or Keysight source measurement unit (B2902A) connected with a probe station (Everbeing Int'l Corp.), where the tungsten tips were used to probe the TE. The voltage bias was given to TE while the BE remained grounded for all the electrical measurements. In addition, impedance analysis was conducted using an Impedance Analyzer (E4990A from Keysight Technologies).

Statistical Analysis: After characterizing the surface morphology using FESEM, the captured images were processed using ImageJ software to outline the individual grains. The grain areas were then measured, and the data were used to generate a histogram distribution, which was plotted using standard Origin software. Moreover, the endurance and retention data were recorded systematically to evaluate the device performance. The resistance values obtained were further analyzed and plotted in Origin software to illustrate their deviation relative to the mean. This was achieved by plotting the percentage of cumulative frequency counts, providing a statistical representation of the data distribution.

Supporting Information

Supporting Information is available from the Wiley Online Library or from the author.

© 2024 Wiley-VCH GmbH

16136829, 2025, 7, Downloaded from https://onlinelibrary.wiley.com/doi/10.1002/smll.202409798 by Indian Institute Of Technology, Wiley Online Library on [05/06/2026]. See the Terms and Conditions (https://onlinelibrary.wiley.com/terms-and-conditions) on Wiley Online Library for rules of use; OA articles are governed by the applicable Creative Commons License

Acknowledgements

A.K. would like to acknowledge the financial support from Shiv Nadar Institution of Eminence, Delhi-NCR and the Science and Engineering Research Board (SERB) Core Research Grant (CRG/2021/001360). A.K. and T.P. would also acknowledge the help received from Dr. P. N. Rao and Dr. S. Rai from BL-2 of RRCAT for their kind help in confirming the phase transition. TP also acknowledges the support of Dr. Raju from Shiv Nadar Institution of Eminence, Delhi-NCR, for performing the FESEM investigation. Dr. Santanu Das (SD) gratefully acknowledges the SERB Core Research Grant (CRG/2022/003204) for providing financial support for this work.

Conflict of Interest

The authors declare no conflict of interest.

Data Availability Statement

The data that support the findings of this study are available from the corresponding author upon reasonable request.

Keywords

cation migration, conductive filament, multilevel resistive switching, self-assembled nanochannel, oxygen vacancy, HfO_2 films

Received: October 21, 2024
Revised: November 25, 2024
Published online: December 5, 2024

[1] S. Ge, X. Guan, Y. Wang, C. Lin, Y. Cui, Y. Huang, X. Zhang, R. Zhang, X. Yang, T. Wu, *Adv. Funct. Mater.* **2020**, *30*, 2002110.
[2] T. S. Lee, N. J. Lee, H. Abbas, H. H. Lee, T.-S. Yoon, C. J. Kang, *ACS Appl. Electron. Mater.* **2020**, *2*, 1154.
[3] J. Bai, W. Xie, W. Zhang, Z. Yin, S. Wei, D. Qu, Y. Li, F. Qin, D. Zhou, D. Wang, *Appl. Surf. Sci.* **2022**, *600*, 154084.
[4] U. Das, D. Das, B. Paul, T. Rabha, S. Pattanayak, A. Kanjilal, S. Bhattacharjee, P. Sarkar, A. Roy, *ACS Appl. Mater. Interfaces* **2020**, *12*, 41718.
[5] Y. Hou, B. Chen, B. Gao, Z. Y. Lun, Z. Xin, R. Liu, L. F. Liu, D. D. Han, Y. Wang, X. Y. Liu, J. F. Kang, In *2013 IEEE Int. Conf. of Electron Devices and Solid-state Circuits*, IEEE: Hong Kong, Hong Kong **2013**, pp. 1.
[6] Z.-Y. He, T.-Y. Wang, L. Chen, H. Zhu, Q.-Q. Sun, S.-J. Ding, D. W. Zhang, *Nanoscale Res. Lett.* **2019**, *14*, 51.
[7] D. Mishra, K. Mokurala, A. Kumar, S. G. Seo, H. B. Jo, S. H. Jin, *Adv. Funct. Mater.* **2023**, *33*, 2211022.
[8] L. Zhao, *Nanoscale* **2014**, *6*, 5698.
[9] J. Lin, S. Wang, H. Liu, *Electronics* **2021**, *10*, 731.
[10] M. H. Jang, R. Agarwal, P. Nukala, D. Choi, A. T. C. Johnson, I.-W. Chen, R. Agarwal, *Nano Lett.* **2016**, *16*, 2139.
[11] M. Qi, C. Guo, M. Zeng, *J. Nanomater.* **2019**, *2019*, 6724018.
[12] M. Kumar, Y. H. Ahn, S. Iqbal, U. Kim, H. Seo, *Small* **2022**, *18*, 2105585.
[13] A. Betal, J. Bera, S. Sahu, *J. Mater. Chem. C* **2023**, *11*, 4674.
[14] E. Covi, S. Brivio, M. Fanciulli, S. Spiga, *Microelectron. Eng.* **2015**, *147*, 41.
[15] A. Betal, A. Chetia, J. Bera, D. Saikia, A. Sharma, A. K. Rath, S. Sahu, *ACS Appl. Nano Mater.* **2024**, *7*, 7226.
[16] A. Mukherjee, S. Sagar, S. Parveen, B. C. Das, *Appl. Phys. Lett.* **2021**, *119*, 253502.
[17] M.-J. Lee, C. B. Lee, D. Lee, S. R. Lee, M. Chang, J. H. Hur, Y.-B. Kim, C.-J. Kim, D. H. Seo, S. Seo, U.-I. Chung, I.-K. Yoo, K. A. F. Kim, *Nat. Mater.* **2011**, *10*, 625.
[18] D. G. Jeong, E. Park, Y. Jo, E. Yang, G. Noh, D. K. Lee, M. J. Kim, Y. Jeong, H. J. Jang, D. J. Joe, J. Chang, J. Y. Kwak, *Chaos Solitons Fractals* **2024**, *183*, 114956.
[19] G. Niu, M. A. Schubert, S. U. Sharath, P. Zaumseil, S. Vogel, C. Wenger, E. Hildebrandt, S. Bhupathi, E. Perez, L. Alff, M. Lehmann, T. Schroeder, T. Niermann, *Nanotechnology* **2017**, *28*, 215702.
[20] C. Chang, J. Chen, C. Huang, C. Chiu, T. Lin, P. Yeh, W. Wu, *Small* **2017**, *13*, 1603116.
[21] H. Jiang, L. Han, P. Lin, Z. Wang, M. H. Jang, Q. Wu, M. Barnell, J. J. Yang, H. L. Xin, Q. Xia, *Sci. Rep.* **2016**, *6*, 28525.
[22] W. Sun, B. Gao, M. Chi, Q. Xia, J. J. Yang, H. Qian, H. Wu, *Nat. Commun.* **2019**, *10*, 3453.
[23] M. Ohring, *Materials Science of Thin Films: Deposition and Structure*, 2nd ed., Academic Press, San Diego, CA **2002**.
[24] S.-S. Lin, C.-S. Liao, S.-Y. Fan, *Surf. Coat. Technol.* **2015**, *271*, 269.
[25] S. Li, Y. Zhang, D. Yang, W. Yang, X. Chen, H. Zhao, J. Hou, P. Yang, *Phys. B Condens. Matter* **2020**, *584*, 412065.
[26] E. Laudadio, P. Stipa, L. Pierantoni, D. Mencarelli, *Crystals* **2022**, *12*, 90.
[27] X. Luo, Y. Li, H. Yang, Y. Liang, K. He, W. Sun, H.-H. Lin, S. Yao, X. Lu, L. Wan, Z. Feng, *Crystals* **2018**, *8*, 248.
[28] A. R. Chourasia, J. L. Hickman, R. L. Miller, G. A. Nixon, M. A. Seabolt, *Int. J. Spectrosc.* **2009**, *2009*, 439065.
[29] S. Kumar, S. B. Rai, C. Rath, *Phys. Chem. Chem. Phys.* **2017**, *19*, 18957.
[30] B. Kim, T. Kang, S. Song, C. Jung, J. Lee, S. Cheon, H. Jeon, *Vacuum* **2022**, *199*, 110957.
[31] T. Dehury, S. Kumar, A. S. Kumar Sinha, M. Gupta, C. Rath, *Mater. Chem. Phys.* **2024**, *315*, 129035.
[32] Int. Conf. on Simulation of Semiconductor Processes and Devices (SISPAD), IEEE, Piscataway, NJ **2014**.
[33] J. Kang, P. Huang, B. Gao, H. Li, Z. Chen, Y. Zhao, C. Liu, L. Liu, X. Liu, *IEEE J. Electron Devices Soc.* **2016**, *4*, 307.
[34] C.-W. Zhong, W.-H. Tzeng, K.-C. Liu, H.-C. Lin, K.-M. Chang, Y.-C. Chan, C.-C. Kuo, P.-S. Chen, H.-Y. Lee, F. Chen, M.-J. Tsai, *Surf. Coat. Technol.* **2013**, *231*, 563.
[35] M. F. Quiñonez, L. Suarez, J. E. Ordoñez, I. C. Arango, M. E. Gomez, W. Lopera, *Mater. Today Proc.* **2019**, *14*, 139.
[36] C. Giovinazzo, J. Sandrini, E. Shahrabi, O. T. Celik, Y. Leblebici, C. Ricciardi, *ACS Appl. Electron. Mater.* **2019**, *1*, 900.
[37] T. Tan, Y. Du, A. Cao, Y. Sun, H. Zhang, G. Zha, *RSC Adv.* **2018**, *8*, 41884.
[38] Q. Chen, G. Liu, W. Xue, J. Shang, S. Gao, X. Yi, Y. Lu, X. Chen, M. Tang, X. Zheng, R.-W. Li, *ACS Appl. Electron. Mater.* **2019**, *1*, 789.
[39] Z. Li, B. Tian, K.-H. Xue, B. Wang, M. Xu, H. Lu, H. Sun, X. Miao, *IEEE Electron Device Lett.* **2019**, *40*, 1068.
[40] O. G. Ossorio, G. Vinuesa, H. García, B. Sahelices, S. Dueñas, H. Castán, E. Pérez, M. K. Mahadevaiah, C.h. Wenger, *ECS J. Solid State Sci. Technol.* **2021**, *10*, 083002.
[41] J. J. Ryu, K. Jeon, S. Yeo, G. Lee, C. Kim, G. H. F Kim, *ACS Appl. Mater. Interfaces* **2019**, *11*, 8234.
[42] R. Marquardt, F. Zahari, J. Carstensen, G. Popkirov, O. Gronenberg, G. Kolhatkar, H. Kohlstedt, M. Ziegler, *Adv. Electron. Mater.* **2023**, *9*, 2201227.
[43] M. Nath, A. Roy, *J. Mater. Sci. Mater. Electron.* **2015**, *26*, 3506.

© 2024 Wiley-VCH GmbH

16136829, 2025, 7, Downloaded from https://onlinelibrary.wiley.com/doi/10.1002/smll.202409798 by Indian Institute Of Technology, Wiley Online Library on [05/06/2026]. See the Terms and Conditions (https://onlinelibrary.wiley.com/terms-and-conditions) on Wiley Online Library for rules of use; OA articles are governed by the applicable Creative Commons License